water

MDPI

Article

Dynamics of Runner and Shafting Vibration Characteristics in a Pump-Turbine Under the Influence of Draft Tube Vortex Rope

Yanhao Li [1], Lei Chen [2], Likun Ding [2] and An Yu [2,*]

[1] Shanghai Investigation, Design & Research Institute Co., Ltd., Shanghai 200335, China; li_yanhao@ctg.com.cn
[2] School of Electrical and Power Engineering, Hohai University, Nanjing 211100, China; chenlei202310@163.com (L.C.); dlk2294269757@163.com (L.D.)
* Correspondence: yu_an@hhu.edu.cn; Tel.: +86-15190490883

Abstract

To investigate the dynamic transmission of unsteady hydraulic excitation within pumped-storage units, this study presents a numerical investigation on the three-dimensional shafting vibrations of a pump-turbine based on a one-way transient fluid-structure interaction approach. To resolve the flow field, we adopt the shear stress transport (SST) k-ω turbulence model in conjunction with the Zwart-Gerber-Belamri (ZGB) cavitation model, and the combined numerical approach is first calibrated against experimental measurements. The results indicate that under the 70% partial load, an eccentric helical vortex rope develops inside the draft tube, generating intense low-frequency pressure pulsations that induce chaotic shaft orbits and distinct orbital drift at the turbine guide bearing. Conversely, near the optimal efficiency point (90% load), the vortex rope transitions into a slender, straight conical core, yielding minimum vibration magnitude and exceptional operational stability. At the 100% rated load, the vortex rope expands into a robust straight conical structure extending continuously into the elbow section. Stress analysis reveals that while equivalent stress concentrations consistently occur at the blade root regions, a reduction in the cavitation number at both 90% and 100% loads leads to a counterintuitive decline in blade surface peak stress values. Additionally, stiffness sensitivity analysis demonstrates that the relative change rates of the shaft runout are highly sensitive to the stiffness variations of the turbine guide bearing, where a stiffness reduction triggers a substantial runout growth of approximately 100% along the X- and Y-directions, whereas the variations in the upper and lower guide bearings exert extremely weak impacts.

Keywords: pump-turbine; draft tube vortex rope; fluid-structure interaction; shafting vibration

Check for updates

Academic Editor: Roberto Gaudio

Received: 1 June 2026
Revised: 3 July 2026
Accepted: 15 July 2026
Published: 19 July 2026

Copyright: © 2026 by the authors. Licensee MDPI, Basel, Switzerland. This article is an open access article distributed under the terms and conditions of the Creative Commons Attribution (CC BY) license.

1. Introduction

In recent years, with the exacerbation of the global energy crisis and the frequent occurrence of extreme weather events, transitioning towards clean and low-carbon energy has become a strategic consensus worldwide. As the energy storage technology with the largest installed capacity and the greatest commercial viability at present, pumped-storage power plants integrate multiple core advantages, including high storage density, low energy conversion loss, an extended life cycle, and a mature engineering technological system. To accommodate the increasingly frequent and stringent flexible regulation demands of the power grid, pump-turbines not only must frequently switch between various operating modes but also inevitably operate under off-design conditions for extended periods. Furthermore, as current pumped-storage units continuously develop towards larger capacities,

higher heads, and higher rotational speeds, the unsteady hydraulic excitation mechanisms within the flow passage have become increasingly intricate. Particularly during operation under off-design conditions, eccentric draft tube vortex ropes are generated within the straight cone section of the draft tube due to the residual circulation in the discharge flow [1]. Concurrently, this hydraulic excitation is further transmitted to the shaft system of the unit, inducing complex torsional, bending, and lateral vibrations within the shaft system [2–4].

In investigating the morphological evolution and cavitation mechanisms of draft tube vortex ropes, scholars have conducted in-depth analyses combining numerical simulations and experimental observations. Liu et al. [5] investigated the vortex rope during the load rejection process of a prototype pump-turbine using numerical simulations, obtaining the fundamental evolution laws of the draft tube vortex rope during this dynamic transient process. Lai et al. [6] experimentally studied the internal flow field of the draft tube in a high-head unit using Laser Doppler Velocimetry (LDV), obtaining precise physical data on the visual morphology and internal velocity distribution of the vortex rope. Kim et al. [7] employed a combined numerical and experimental approach to study the characteristics of inter-blade vortices and the draft tube vortex rope at low flow rates, revealing the spatial correlation between flow separation within the flow passage and the downstream evolution of the vortex rope. Based on the Shear Stress Transport (SST) k-ω turbulence model, He et al. [8] investigated the draft tube vortex rope of a pump-turbine under various operating conditions, identifying the distribution patterns of coherent vortex structures in the internal flow field during off-design operation. Lai et al. [1] combined LDV and high-speed photography to investigate the draft tube flow field of a pump-turbine with splitter blades, obtaining the physical evolution laws of the complex cavitating vortex rope.

Moreover, to more accurately capture the topological structures of the vortex rope and evaluate the induced energy losses, various vortex identification methods and entropy production theory have been widely applied. Wang et al. [9] investigated the hydraulic losses within the draft tube vortex rope of a Francis pump-turbine based on entropy production theory, obtaining the specific spatial distribution and quantitative proportions of energy dissipation during the vortex rope evolution. Yu et al. [10] conducted an in-depth analysis of the internal flow in a variable-speed pump-turbine utilizing the SST k-ω turbulence model and the Liutex vortex identification method, finding that variable-speed operation can effectively reduce the pressure pulsation amplitude of the unit by approximately 20% to 30%. Furthermore, reduced-order modeling techniques for flow fields have deepened the research on vortex rope mechanisms. Liu et al. [11] adopted Proper Orthogonal Decomposition (POD) and Dynamic Mode Decomposition (DMD) methods to study the coherent structures of the twin-helical vortex rope under low-load conditions, and they successfully reconstructed the high-order spatiotemporal evolution as well as the dominant frequency components of this intricate flow field.

Subsequently, numerous scholars have focused on excitation factors such as cavitation and vortex ropes, conducting research on the deterioration of the internal flow field and the structural loading characteristics of the runner under off-design conditions. Zhu et al. [12] employed the detached eddy simulation (DES) method and the Zwart-Gerber–Belamri (ZGB) cavitation model, revealing the nonlinear trend that the axial hydraulic thrust first increases and then sharply decreases during the evolution from non-cavitation to critical cavitation. Hou et al. [13] utilized the scale-adaptive simulation based on the shear stress transport model (SAS-SST) turbulence model to capture the dynamic evolution of the clearance flow field, concluding that the severe fluctuations of the clearance flow significantly alter the loading state of the runner. Following comparative analyses, Xin et al. [14] selected the SST k-ω turbulence model for numerical simulations and discovered that as

the unit operates deeper into the S-region, the clearance flow pattern evolves from pure axial leakage to highly three-dimensional turbulent distortion, thereby exerting extremely intense hydraulic loads on the runner. Furthermore, to accurately evaluate the structural safety of the runner, fluid-structure interaction (FSI) technology has become an indispensable analytical tool. Chen et al. [15] coupled one-dimensional (1D) pipeline calculations with three-dimensional (3D) computational fluid dynamics (CFD) simulations to obtain the dynamic stress distribution results of the runner during the unit startup process. Additionally, employing a two-way FSI analysis, Li et al. [16] found that substantial fluctuations in the operating head greatly exacerbate the vibration response of the runner. Guo et al. [17] investigated through numerical simulations how hydraulic excitation during the transient process intensifies the amplitude fluctuations of blade dynamic stress.

The shaft system of a pump-turbine is primarily constrained by bearings; thus, the bearing structure is also a crucial factor to consider. Lund [18] integrated traditional rotor dynamics with the principles of bearing lubrication dynamic characteristics to establish a rotor-bearing model. Furthermore, by combining experimental methods with fluid dynamics research, several scholars [19,20] have proposed novel dynamic characteristic models for bearings. Comparative results demonstrate that these models can effectively capture the dynamic behaviors of rotating machinery in practical applications.

In the finite element modeling (FEM) and dynamic characteristics evaluation of unit shaft systems, the research paradigm has evolved from isolated structural analysis toward the coupled analysis of multiple nonlinear physical factors. Pandya et al. [21] confirmed the significant role of finite element analysis in solving natural frequencies and conducting modal analyses of shaft systems through a systematic literature review. Meanwhile, Liu et al. [22] horizontally compared different numerical algorithms for the modal analysis of pump-turbine shaft systems, clarifying the high sensitivity of fluid-structure interaction modal results to variations in boundary conditions. Following fundamental investigations into structural modes, the additional physical effects induced by complex operating environments have gradually become a research focus. Cao et al. [23] introduced the hydrodynamic added mass and gyroscopic effects into wet modal calculations, revealing a peculiar shift phenomenon in the mode shapes of the shaft system under the coupled influence of these two effects. Focusing on variable-speed units, Wang et al. [24] elucidated the influence patterns of continuously varying rotational speeds on the inherent modal distribution and resonance margins of the rotor system.

Finally, under partial load and complex transient operating conditions, severe hydraulic excitation is often the core factor inducing shaft system instability. Through structural analysis, Kong et al. [25] discovered that the shaft system exhibits asymmetric deformation in both axial and radial directions. Mao et al. [26] investigated the evolution characteristics of the axial hydraulic thrust during the initial stage of startup in pump mode, pointing out that specific low-frequency hydraulic pulsations and unbalanced forces are the direct driving forces for early shaft system vibrations. Adopting a 1D-3D coupled multi-excitation transient computational framework, Feng et al. [27] studied the vibration characteristics of the shaft system during transient processes such as load rejection. They concluded that the sudden increase in radial vibration highly corresponds with runner stall, and the shaft orbit becomes more chaotic and complex under multi-field coupling. Zhou et al. [28] constructed a vibration model incorporating nonlinear fluid film forces and unbalanced magnetic pull, elucidating the nonlinear perturbation laws of multi-source excitations on the rotor. The applied research by Zhang et al. [29] also confirmed the existence of strong nonlinear energy transfer among various subsystems during the startup transient process. In a multidimensional coupled nonlinear dynamic model, Shi et al. [30] innovatively introduced a state feedback control strategy, theoretically demonstrating that

active intervention methods exert excellent effects on suppressing the nonlinear vibration of the shaft system.

A review of the extensive literature reveals that the stability of the unit has become a prominent research focus in the field of pump-turbines in recent years. However, the majority of studies concerning vibration characteristics are confined to pure mathematical models, with only a select few investigating stability by applying explicit excitation forces to an isolated solid domain model. The draft tube vortex rope, acting as the most critical hydraulic excitation factor, plays a pivotal role in the operational stability of the unit; nevertheless, existing research on the vortex rope is predominantly concentrated solely within the fluid domain. Consequently, it remains relatively rare to analyze vibration characteristics by applying the real-time calculated hydraulic excitation forces of the pump-turbine to a three-dimensional shaft system model utilizing the fluid-structure interaction method.

Therefore, given the current engineering context in which pumped-storage units frequently operate under off-design conditions, this study integrates CFD and FEM to conduct numerical simulations on the three-dimensional shaft system vibration of the pump-turbine. These simulations are carried out by employing the SST k-ω turbulence model, the ZGB cavitation model, and a one-way transient FSI approach, with their accuracy rigorously ensured through experimental validation. Based on the numerical simulation results, this study explores the evolution process and formation mechanism of the draft tube vortex rope, and further investigates the correlations among the draft tube vortex rope, runner dynamics, and shaft system vibration, thereby laying a solid foundation for the stable operation of pumped-storage power plants.

This paper proceeds as follows: Section 2 introduces the mathematical models, including the governing equations, the turbulence model, and the cavitation model. Section 3 details the CFD configurations, encompassing the physical model, mesh model, boundary conditions, and experimental validation. The numerical results are reported in Section 4, and the main conclusions are drawn in Section 5.

2. Mathematical Model

Thermal effects are generally negligible during the internal flow of pump-turbines. For this reason, the energy equation is excluded from the current model. The flow field is governed solely by the conservation laws of mass and momentum. Additionally, the working medium is treated as a strictly incompressible fluid with a constant density. Based on these physical assumptions, the basic governing equations are formulated as follows:

$$\frac{\partial \rho}{\partial t} + \frac{\partial (\rho U_j)}{\partial x_j} = 0 \tag{1}$$

$$\frac{\partial (\rho U_i)}{\partial t} + \frac{\partial (\rho U_i U_j)}{\partial x_j} = -\frac{\partial P}{\partial x_i} + \frac{\partial}{\partial x_j}\left[(\mu + \mu_{tur}) \left(\frac{\partial U_i}{\partial x_j} + \frac{\partial U_j}{\partial x_i} - \frac{2}{3} \frac{\partial U_k}{\partial x_k} \delta_{ij} \right) \right] \tag{2}$$

In these equations, the symbols ρ, U, P, and t indicate the fluid density, time-averaged velocity, pressure, and time, respectively, while μ and μ_{tur} stand for the dynamic and turbulent viscosities.

Large Eddy Simulation (LES) accurately resolves small-scale eddies, but its immense computational cost prohibits its application across numerous operating conditions. Meanwhile, the standard k-ε model [31] and standard k-ω models are discarded owing to their inherent deficiencies in near-wall treatments and computational economy. By incorporating the transport of principal turbulent shear stress, the SST k-ω turbulence model significantly outperforms the standard version in predicting adverse pressure gradients and wake vor-

tices. Consequently, the SST k-ω turbulence model is selected for the present simulations. Its transport equations for k and ω are expressed as follows:

$$\frac{\partial k}{\partial t} + \overline{u_j}\frac{\partial k}{\partial x_j} = P_k + \frac{\partial}{\partial x_j}\left[(\nu + \sigma_k \nu_t)\frac{\partial k}{\partial x_j}\right] - \beta^* k\omega \tag{3}$$

$$\frac{\partial \omega}{\partial t} + \overline{u_j}\frac{\partial \omega}{\partial x_j} = \alpha S^2 - \beta\omega^2 + \frac{\partial}{\partial x_j}\left[(\nu + \sigma_{\omega 1}\nu_t)\frac{\partial \omega}{\partial x_j}\right] + 2(1 - F_1)\sigma_{\omega 2}\frac{1}{\omega}\frac{\partial k}{\partial x_i}\frac{\partial \omega}{\partial x_i} \tag{4}$$

The expression for F_1 is as follows:

$$F_1 = \tanh\left\{\left\{\min\left[\max\left(\frac{\sqrt{k}}{\beta^*\omega y}, \frac{500\nu}{y^2\omega}\right), \frac{4\sigma_{\omega 2}k}{CD_{k\omega}y^2}\right]\right\}^4\right\} \tag{5}$$

$$CD_{k\omega} = \max\left(2\rho\sigma_{\omega 2}\frac{1}{\omega}\frac{\partial k}{\partial x_i}\frac{\partial \omega}{\partial x_i}, 10^{-10}\right) \tag{6}$$

Turbulent viscosity is defined as:

$$\nu_t = \frac{\alpha_1 k}{\max(\alpha_1\omega, SF_1)} \tag{7}$$

In this blending function, F_1 accounts for the weighting between the two turbulence models across the computational domain, with Y indicating the wall distance. The empirical coefficients β^*, $\sigma\omega_1$, and $\sigma\omega_2$ are taken as 0.09, 0.5, and 0.856, respectively, following experimental calibration.

The ZGB model exhibits exceptional adaptability for simulating cavitating flows in ambient-temperature water. This framework is extensively applied throughout the field of hydraulic turbomachinery, consistently yielding predictions that align well with empirical measurements [32,33]. Consequently, the present research adopts the ZGB approach to govern all relevant multiphase numerical computations.

$$m^+ = C_e\frac{3p_v\alpha_{nuc}(1 - \alpha_v)}{R_b}\sqrt{\frac{2}{3}\frac{Max(p_v - p, 0)}{\rho_1}} \tag{8}$$

$$m^- = C_c\frac{3p_v\alpha_v}{R_b}\sqrt{\frac{2}{3}\frac{Max(p_v - p, 0)}{\rho_1}} \tag{9}$$

In the equation, R_b denotes the bubble radius, while p and p_v are the local fluid pressure and the saturated liquid vapor pressure, respectively.

3. Computational Model and Numerical Setup

3.1. Numerical Simulation Settings

The current research focuses on a scaled pump-turbine model. The entire computational fluid domain incorporates five primary components: the volute, stay vanes, guide vanes, runner, and draft tube. The three-dimensional configuration of the unit is shown in Figure 1. Additionally, Table 1 outlines its fundamental design parameters.

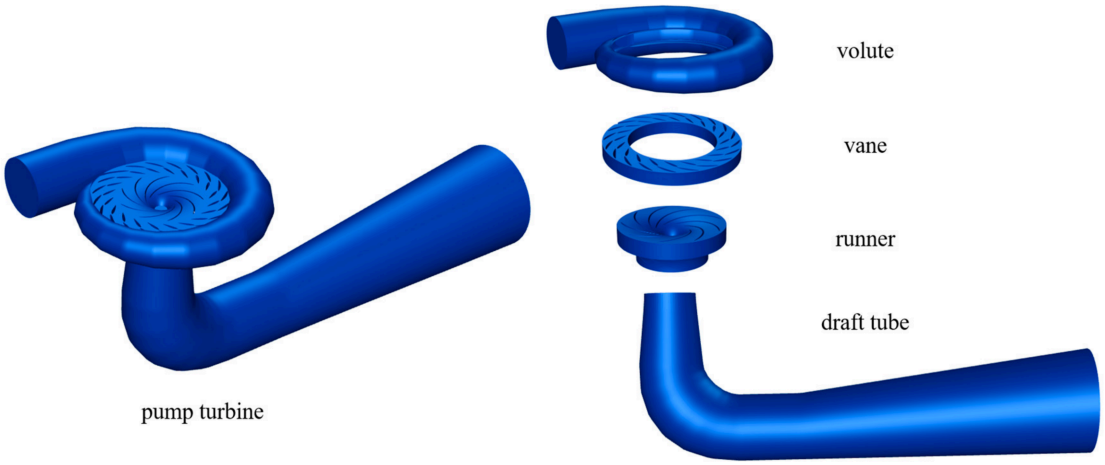


Figure 1. Physical model of a pump turbine.

Table 1. Basic parameters of a pump turbine.

Parameter	Value
Runner inlet diameter D_2	0.442 m
Runner outlet diameter D_1	0.3 m
Number of runner blades	9
Number of stay vanes	20
Number of guide vanes	20
Rate rotation speed	1500 r/min
Draft tube height	1.1092 m
Draft tube length	2.4723 m

Structured hexahedral meshes are generated for the entire computational fluid domain. Local mesh refinement is strictly implemented near all solid walls to accurately capture the boundary-layer flows. Figure 2 depicts the detailed mesh distribution. Furthermore, general mesh interfaces connect the adjacent sub-domains. The mesh densities on both sides of these paired surfaces are carefully matched. This spatial consistency effectively minimizes interpolation errors during data transmission across the boundaries.

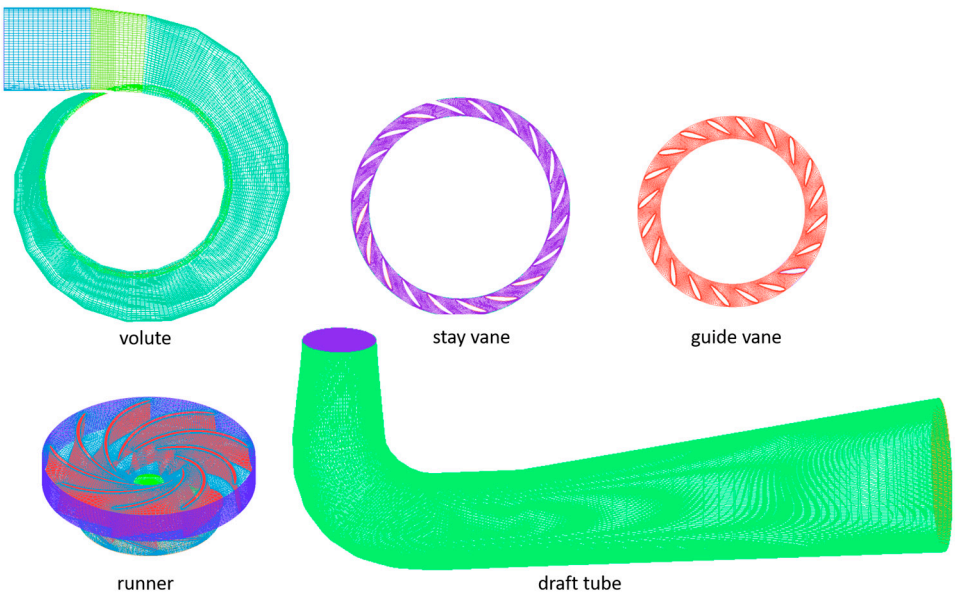


Figure 2. Computational domain mesh.

The commercial CFD solver ANSYS Fluent 2022 R1 is employed to perform all numerical computations. The entire computational procedure consists of both steady-state and transient analyses. To accelerate convergence, the fully developed steady-state flow field serves as the initial condition for the subsequent unsteady simulations. The SST k-ω turbulence model is adopted to close the governing equations. This model excellently handles adverse pressure gradients and flow separation. Consequently, it is highly suitable for capturing the complex internal flow structures within the pump-turbine. Furthermore, the Mixture multiphase framework is coupled with the ZGB cavitation model to accurately resolve the intricate cavitating flow features. Regarding boundary conditions, a total pressure inlet and a static pressure outlet are prescribed. All solid boundaries are strictly enforced with no-slip wall conditions. Finally, the convergence criterion for all equation residuals is set to 1×10^{-4}.

Six representative operating conditions are selected for the current numerical investigations. Table 2 lists the detailed operational parameters. The evaluated power loads increase progressively from 70% to 100%. For all simulated cases, the operating head is strictly maintained at the rated value of 50 m. The internal flow rate is controlled purely by adjusting the guide vane opening. This specific adjustment consequently determines the active power output of the unit. Additionally, the cavitation number under each load scenario is regulated by modifying the static pressure at the outlet. The mathematical definition of this coefficient is expressed as follows:

$$\sigma = \frac{\frac{P_{out} - P_v}{\rho g} - H_s}{H} \tag{10}$$

The outlet pressure of the draft tube is given by P_{out} (in Pa), and the suction head of the turbine is H_s = 1 m. The operating head H is 50 m, while P_v is the saturated vapor pressure at 25 °C, which equals 3540 Pa.

Table 2. Operational parameters of the pump-turbine under representative conditions.

Load Level	Flow Rate (m^3/s)	Guide Vane Opening (°)	Head (m)	Cavitation Number
70%Pr	0.432	22.5	50	0.09
	0.432	22.5	50	0.06
90%Pr	0.548	30.6	50	0.09
	0.548	30.6	50	0.06
100%Pr	0.625	37.3	50	0.09
	0.625	37.3	50	0.06

Figure 3 illustrates the geometric model of the pump-turbine shaft system. The computational solid domain comprises the main shaft, the thrust bearing, the upper and lower guide bearings, the turbine guide bearing, the generator rotor, and the runner. This structural assembly undergoes a rational simplification for the numerical analysis. Specifically, only the rotating components physically attached to the main shaft are retained in the 3D modeling. Furthermore, the physical supporting effects of the actual bearings on the global shaft system are equivalently represented. Appropriate boundary constraints are applied directly to the corresponding bearing surfaces based on their equivalent stiffness coefficients.

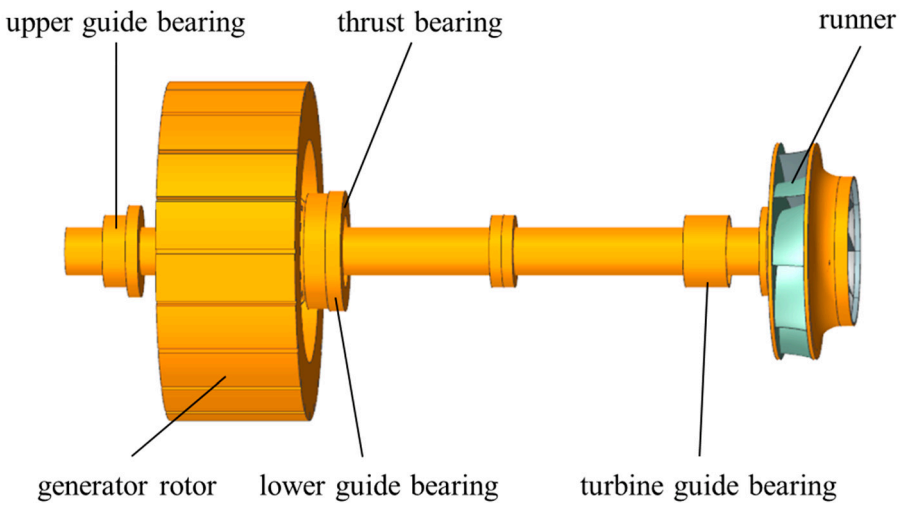


Figure 3. Three-dimensional (3D) model of the pump-turbine shaft system.

Unstructured meshes are generated for the solid domain using the integrated meshing tool within ANSYS Workbench 2022 R1. Figure 4 displays the corresponding mesh topology. Because the runner blades serve as the fluid–structure interaction interface to transfer pressure data between the fluid and solid domains, local mesh refinement is implemented in the runner section. Similarly, the mesh density around the bearings is locally increased since these components represent the critical locations for monitoring shaft system displacements. Following a mesh independence validation, the final total element count for the solid model is established at approximately 0.6 million.

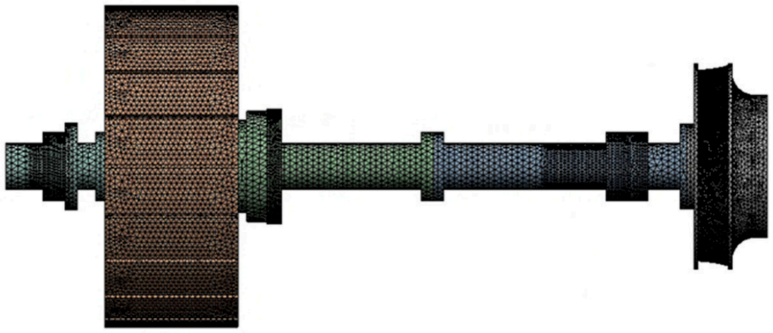


Figure 4. Mesh of the solid domain.

The one-way transient FSI analysis is performed using the ANSYS Workbench 2022 R1 platform. This numerical procedure couples three core modules: Fluent, Transient Structural, and System Coupling. Radial vibrations of the shaft are restricted by three guide bearings. These mechanical boundaries are simulated by applying 'Bearing Connections' directly to the corresponding surfaces. Specifically, the radial stiffness values for the turbine, lower, and upper guide bearings are defined as 1.2×10^7 N/m, 3.5×10^7 N/m, and 4.7×10^7 N/m, respectively. In contrast, the thrust bearing is responsible for suppressing axial vibrations. This constraint is introduced via 'Spring Connections' with a specified axial stiffness of 3.0×10^9 N/m. In addition, the damping coefficient for each guide bearing is set to 1% of the stiffness coefficient. For the remaining structural conditions, the rotational speed of the assembly is fixed at 1500 rpm, and a constant gravitational acceleration of 9.8066 m/s^2 is activated. Finally, the runner blades are explicitly designated as the FSI data-exchange interfaces. This configuration guarantees the precise transmission of hydrodynamic pressures from the fluid domain to the solid structure.

3.2. Numerical Simulation Verification

The mesh resolution significantly influences the reliability of CFD simulations. An excessively dense mesh incurs prohibitive computational costs. Conversely, an overly coarse mesh compromises numerical accuracy. Therefore, an optimal element count must be determined to balance computational efficiency and simulation fidelity. Seven distinct meshing schemes are evaluated to perform the mesh independence test. Table 3 lists the specific element counts for each scheme. Numerical simulations under the design operating condition are independently conducted for all configurations. Figure 5 presents the verification results. The internal flow rate stabilizes at approximately 634 L/s once the total mesh count reaches 4.51 million. This specific resolution successfully meets the precision requirements while conserving computational resources. Consequently, the mesh containing 4.51 million elements is finalized for the formal computations. With Scheme 6 chosen for the subsequent simulations, the mean y^+ values on both the runner blades and the guide vanes are kept well below 30. This near-wall mesh distribution satisfies the theoretical requirements of the adopted turbulence model. In all other fluid regions, the maximum y^+ value does not exceed 80.

Table 3. Mesh schemes.

Scheme	1	2	3	4	5	6	7
Mesh count ($\times 10^6$)	1.52	2.01	2.58	3.15	3.87	4.51	6.02

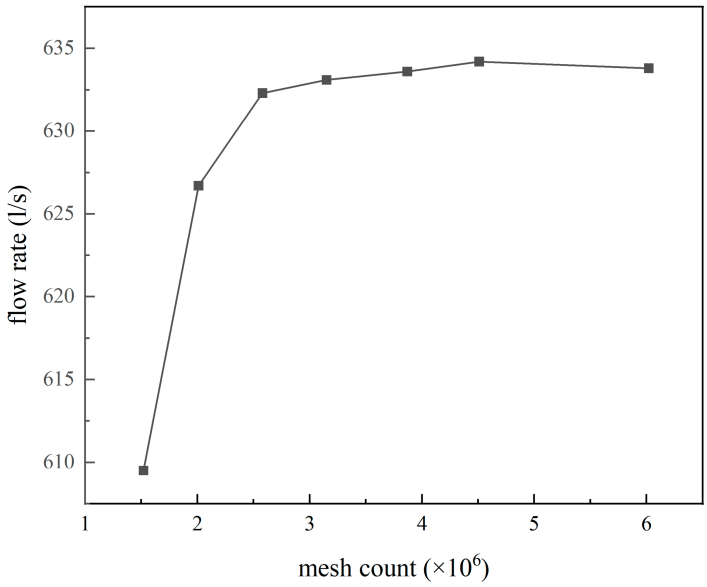


Figure 5. Mesh independence validation.

A time step independence test is conducted to ensure the reliability of the transient results. Specifically, the pressure fluctuations in the vaneless space are compared under the 70% load condition. Three distinct time step sizes are evaluated: 2×10^{-4} s, 4×10^{-4} s, and 6×10^{-4} s. Figure 6 displays the corresponding comparative results. The overall transient trends remain highly consistent across all three cases. However, a smaller time interval yields superior accuracy in capturing the peak fluctuation values. Consequently, the final time step is strictly set to 2×10^{-4} s. This temporal resolution corresponds to approximately 1.8° of runner rotation. During the actual unsteady simulations, an initial time step of 6×10^{-4} s is applied to accelerate the early flow development. Once the macroscopic flow field stabilizes, the time step is refined to 2×10^{-4} s for the formal computations.

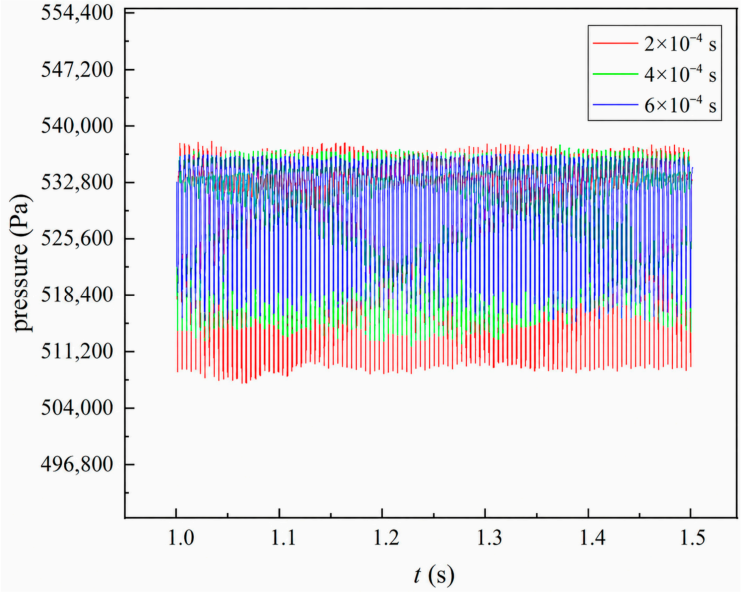


Figure 6. Time step independence verification.

The numerical results across various power loads are systematically compared with experimental data to validate the accuracy of the CFD simulations. Figure 7 illustrates this comprehensive comparison. The predicted efficiency trend aligns consistently with the experimental measurements. Generally, the numerically calculated efficiency is marginally lower than the experimental value. However, the maximum relative error remains strictly confined within 1%. Furthermore, the pressure fluctuation characteristics within the vaneless space and the draft tube are rigorously validated. The 70% load condition is specifically selected for this transient verification. Figure 8 presents these detailed comparative results. Specifically, the top and bottom rows correspond to the experimental and numerical data, respectively. A detailed spectral comparison reveals that the predicted dominant frequencies at the monitoring points are slightly higher. Nevertheless, they still exhibit a satisfactory agreement with the experimental measurements. In conclusion, the numerical predictions agree favorably with the experimental data, thereby confirming the reliability and rationality of the adopted numerical methodology.

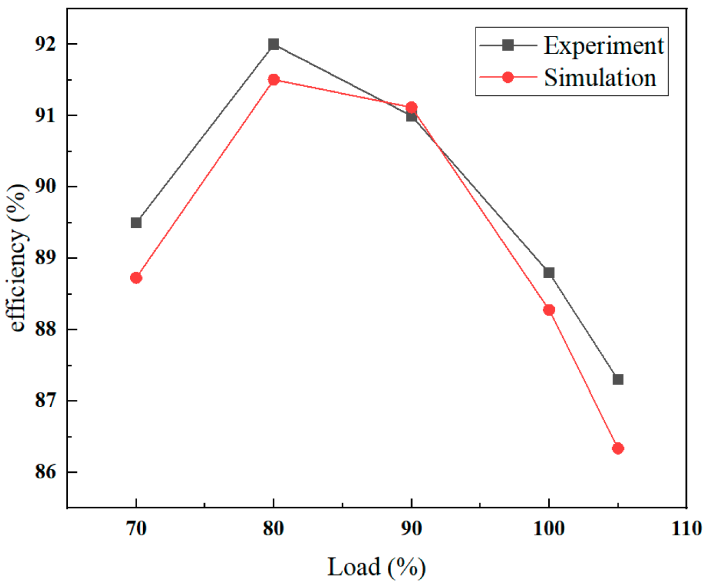


Figure 7. Comparison of experimental results and numerical simulation results.

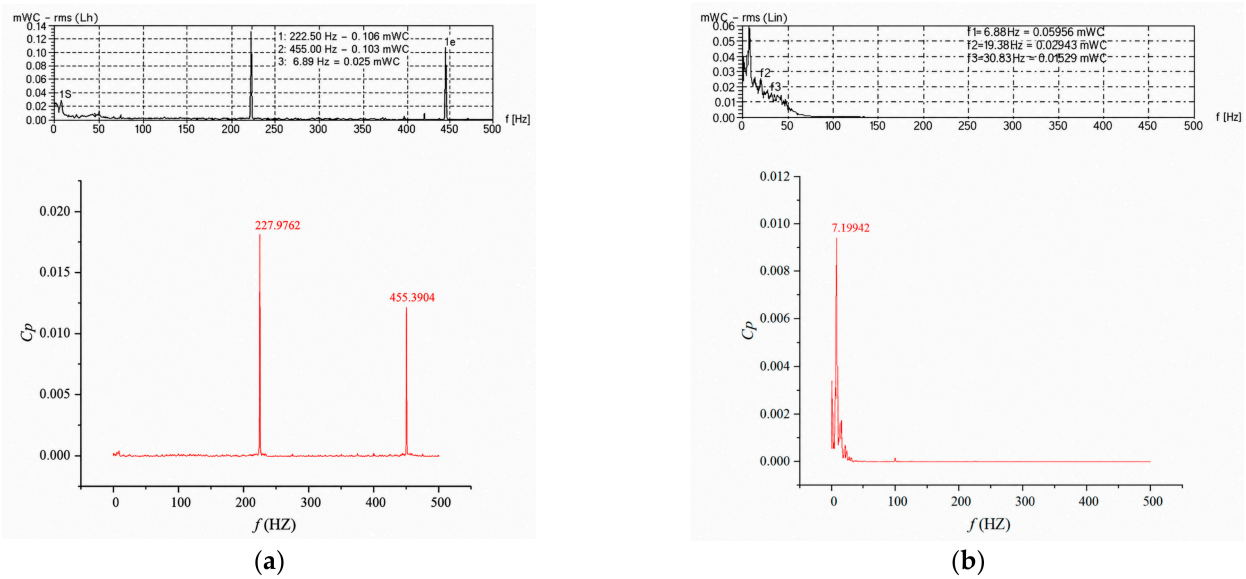


Figure 8. Comparison between the numerical and experimental pressure fluctuations: (**a**) Vaneless space; (**b**) Draft tube.

4. Results and Discussion

4.1. Flow Field Characteristics in the Draft Tube

Figures 9–11 illustrate the pressure contours and streamline distributions on the *XZ* cross-section (*Y* = 0 m) of the draft tube under various operating conditions. As observed in Figure 9, the internal flow field exhibits a highly unstable state under the 70% load condition. Focusing initially on the streamline patterns, extremely complex and distorted flow structures emerge within the straight cone section. Specifically, multiple closed streamline configurations appear in the central region. Subsequent examination of the pressure contours reveals a massive low-pressure zone within this straight cone area. Notably, this low-pressure core undergoes an eccentric displacement along the axial direction. Furthermore, a comparison of the flow patterns across different cavitation numbers reveals a distinct trend: the total spatial extent of the low-pressure zone expands significantly as the cavitation number decreases.

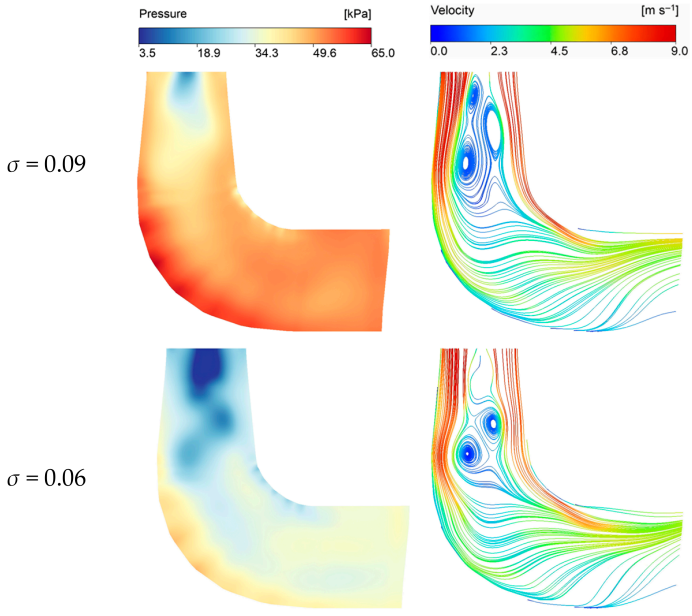


Figure 9. Pressure and streamline distributions on the *ZX* plane at 70% load.

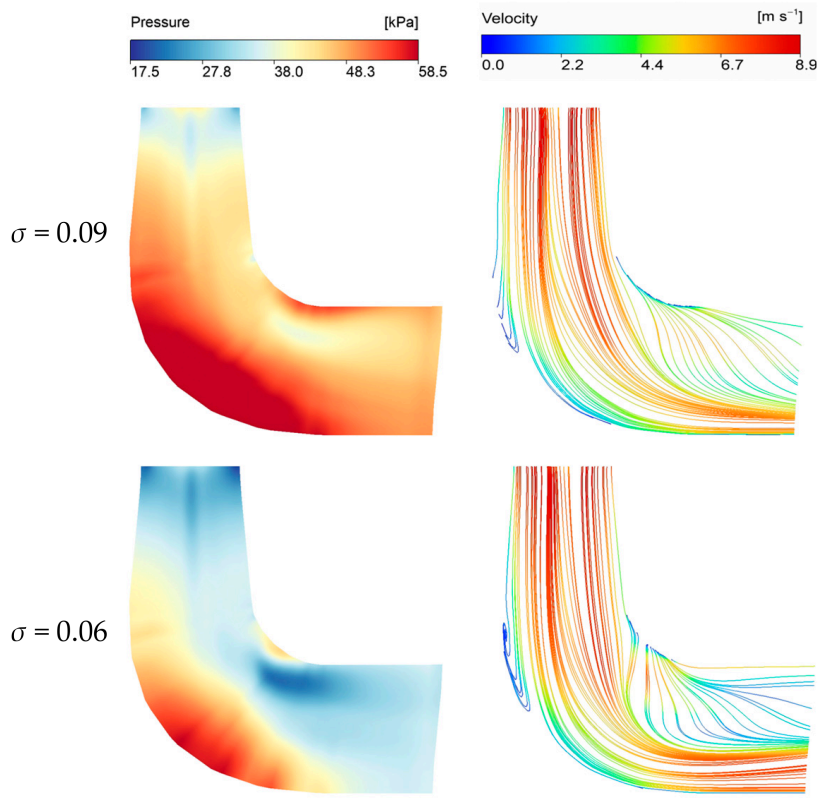


Figure 10. Pressure and streamline distributions on the *ZX* plane at 90% load.

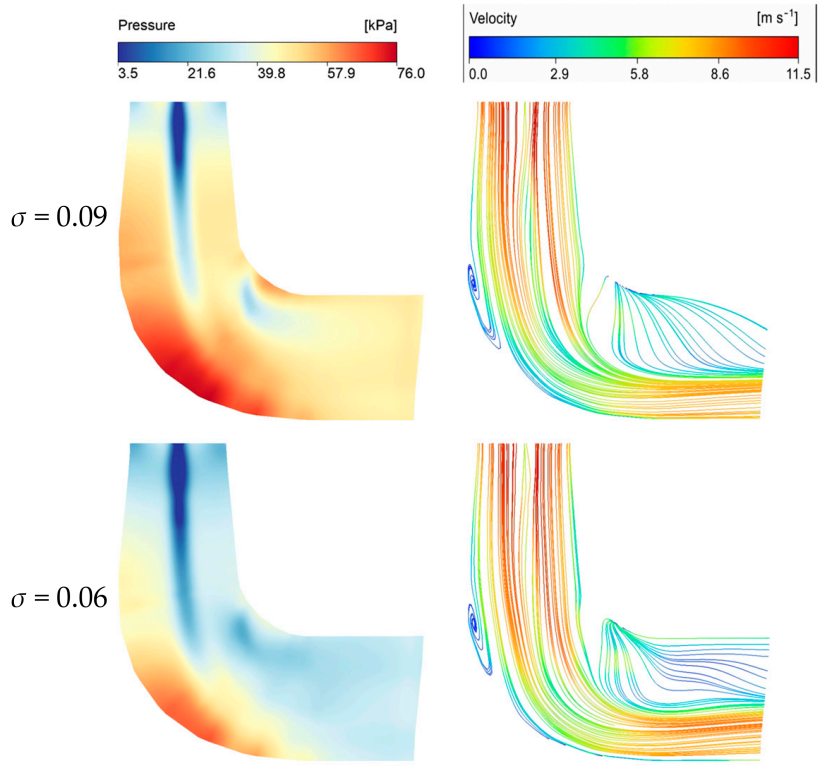


Figure 11. Pressure and streamline distributions on the *ZX* plane at 100% load.

At the 90% load condition, the unit operates near its optimal efficiency point. Consequently, the internal flow field remains highly stable. As depicted by the streamline patterns in Figure 10, the fluid within the straight cone section follows extremely smooth axial trajectories. No obvious flow blockage zones are observed. However, localized flow

deflection and separation phenomena occur near the inner wall of the elbow section where the fluid changes direction. This is primarily attributed to the significant inertial forces acting on the high-speed fluid as it navigates the curved boundary, which inevitably triggers flow separation. An examination of the corresponding pressure contours indicates that the minimum pressure for this specific case is approximately 17.5 kPa. Overall, the pressure distribution throughout the straight cone section is remarkably uniform. Only a slender low-pressure band emerges in the central core of the straight cone. Concurrently, a minor low-pressure pocket forms exactly at the flow separation region. As the cavitation number decreases, the macroscopic stability of the flow field remains entirely unaffected. Although the global pressure values drop accordingly, they consistently stay well above the critical vaporization pressure.

Figure 11 depicts the flow field distributions within the draft tube under the 100% load condition. Based on the streamline patterns, the entire straight cone section is dominated by a high-speed downward axial flow. Furthermore, the streamline deflection and detachment near the inner wall of the elbow section become markedly more severe. This indicates that a significantly more pronounced flow separation phenomenon occurs in this specific region. An examination of the pressure contours reveals a straight, columnar low-pressure zone exactly in the center of the flow field. This distinct core structure penetrates the entire length of the straight cone section. However, unlike the eccentric low-pressure region observed under the 70% load condition, this entire zone exhibits a high degree of structural symmetry. Moreover, it extends continuously down to the bottom of the draft tube. A subsequent comparison across different cavitation numbers reveals an additional characteristic. As the cavitation number decreases, the central columnar low-pressure zone undergoes a discernible radial expansion.

To further investigate the morphological variations of the vortex rope within the draft tube, the second-generation vortex identification method, specifically the Q-criterion, is employed. The Q-criterion is then used to capture the spatial–temporal development of the vortex rope in the draft tube under different operating and cavitation conditions. For these three-dimensional visualizations, the corresponding iso-surface value of the Q-criterion is precisely defined as 3000 s^{-2}. The Q-criterion identifies vortex core structures by detecting regions where the square of the modulus of the rotation tensor ($\mathbf{\Omega}$) is greater than the square of the modulus of the strain rate tensor ($\mathbf{S}$). This method is more effective for extracting coherent structures in the wake vortices of water pipes. The specific formula is as follows:

$$Q = \frac{1}{2}\left(\|\Omega\|^2 - \|S\|^2\right) \tag{11}$$

Figure 12 presents the velocity vector distributions and the spatiotemporal evolution of the vortex rope within the draft tube under the 70% load condition. Regarding its spatial morphology, a prominent helical vortex rope is generated inside the draft tube. This phenomenon is primarily driven by the intense residual swirl discharging from the runner exit. By observing a complete period from time T1 to T5, it is evident that this eccentric helical vortex rope undergoes periodic rotation and stretching motions. Furthermore, a comparison of the vortex evolution across varying cavitation numbers reveals a critical mechanism. The occurrence of cavitation actively promotes the development and kinematics of the vortex rope. Consequently, the overall structure of the vortex rope experiences a distinct volumetric expansion.

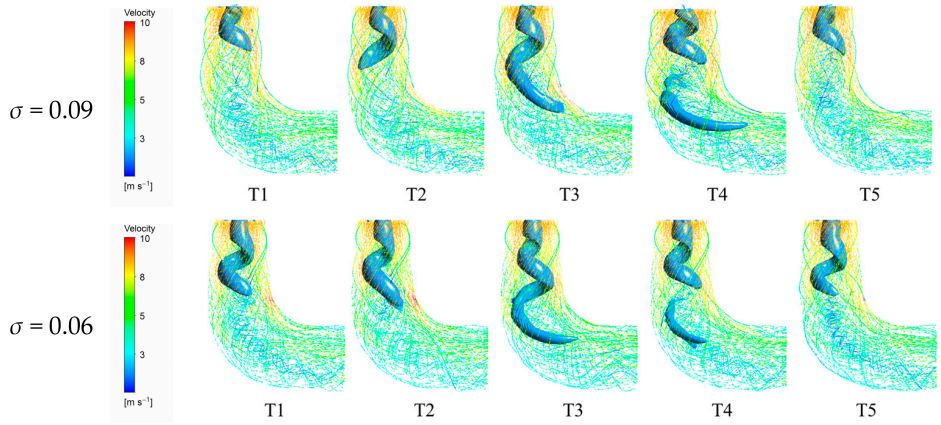


Figure 12. Draft tube velocity vectors and vortex rope evolution at 70% load.

Figure 13 illustrates the velocity vectors and the evolution of the vortex rope in the draft tube at the 90% load condition. Since the unit operates near its optimal efficiency point, the residual swirl of the flow discharging from the runner exit is extremely minimal. Consequently, the vortex rope manifests as a slender, straight conical structure. Throughout the entire evolution cycle, the axial length of the vortex rope remains largely constant. The structure merely undergoes a periodic rotation around the centerline of the draft tube. Furthermore, an observation of the evolution process across various cavitation numbers reveals that both the morphology and length of the vortex rope are virtually unaltered. This demonstrates that cavitation exerts a negligible influence on the vortex rope under this specific operating condition.

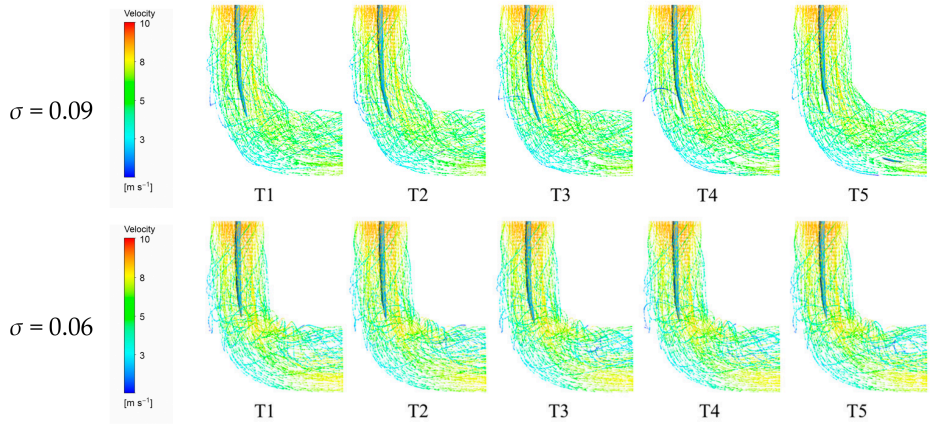


Figure 13. Draft tube velocity vectors and vortex rope evolution at 90% load.

Figure 14 presents the velocity vectors and the evolution of the vortex rope in the draft tube under the 100% load condition. As observed from the vortex structures, an increase in the guide vane opening leads to a higher flow rate. Consequently, the fluid discharging from the runner exit regains a substantial residual swirl. This hydrodynamic shift causes the previously slender vortex rope, which was observed at the 90% load, to expand rapidly. It ultimately develops into a robust, straight conical vortex structure. Throughout the entire evolution cycle, this vortex rope not only rotates around the draft tube centerline but also experiences periodic elongation and contraction in its axial length. Notably, due to the augmented flow rate and the correspondingly high axial velocity, this vortex rope does not rupture within the elbow section—a phenomenon previously observed under the 70% load condition. Instead, it extends continuously deep into the elbow passage. Finally, a comparison across various cavitation numbers indicates that a lower cavitation number

moderately increases both the length and volume of the vortex rope. However, because the vortex rope consistently rotates strictly around the centerline, this volumetric expansion does not trigger any macroscopic flow instability.

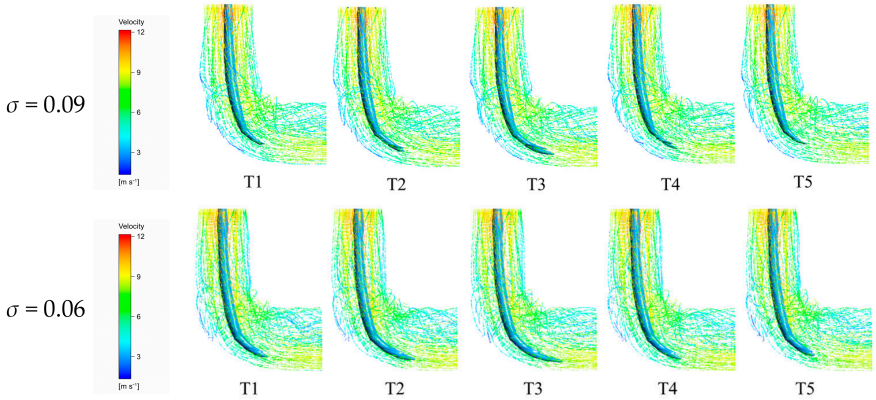


Figure 14. Draft tube velocity vectors and vortex rope evolution at 100% load.

The preceding section utilizes the Q-criterion to illustrate the draft tube vortex rope structures under various operating loads. To further explore the intensity and spatial distribution of the cavitation phenomenon, this study identifies the three-dimensional cavitation vapor pockets within the draft tube via iso-surfaces defined by a vapor volume fraction of 0.1. Figure 15 presents the three-dimensional cavitation vapor morphologies within the draft tube under various loads and cavitation numbers. Regarding the 70% partial load condition, no cavitation inception is observed within the straight cone section under the high cavitation number; however, as the cavitation number decreases to 0.06, a substantial, irregularly shaped cavitation vapor cavity emerges, whose structural irregularity is precisely driven by the previously discussed eccentric helical vortex rope. Upon transitioning to the 90% load condition, no discernable cavitation vapor pockets are captured inside the draft tube under either cavitation number. This outcome highlights that the internal flow remains exceptionally smooth with no pronounced low-pressure zones, confirming that the unit operates at its optimal hydraulic stability across all evaluated scenarios. Finally, examining the 100% rated load condition, the cavitation phenomenon reoccurs within the draft tube as the load increases; nevertheless, the morphology of the cavitation vapor pockets exhibits a high degree of symmetry. Under this 100% load condition, the cavitation vapor pocket manifests as a slender, straight conical core extending continuously downstream along the central flow path, which undergoes a distinct radial expansion as the cavitation number drops.

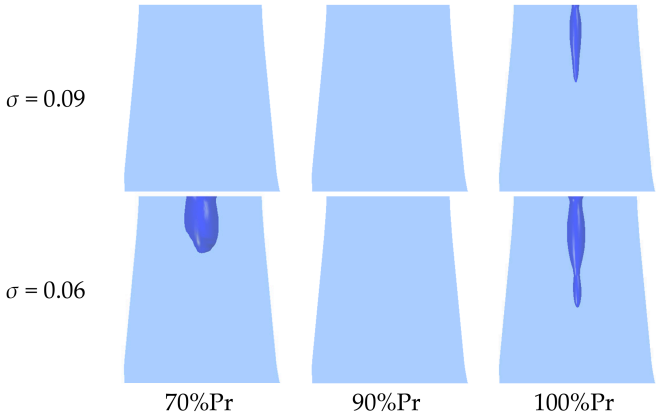


Figure 15. Distribution of cavitation vapor volume within the draft tube under various operating conditions.

Based on the analysis of the internal flow field within the draft tube in this section, it is found that under the 70% partial load condition, an eccentric helical vortex rope is formed due to the influence of the residual swirl at the runner exit and the shed vortices. Consequently, both the pressure field and streamline patterns exhibit extreme asymmetry. When the unit operates at the 90% load condition, the internal fluid manifests as an exceptionally smooth axial discharge; however, a slight flow separation phenomenon occurs near the inner wall of the elbow section. With a further increase in the flow rate, a symmetric columnar low-pressure zone emerges at the center of the draft tube under the 100% load condition, extending continuously into the elbow section. Concurrently, the flow separation phenomenon becomes notably more severe as the high-speed fluid navigates through the elbow passage. Across all evaluated load conditions, a reduction in the cavitation number consistently induces a certain degree of volumetric expansion in the vortex rope.

4.2. Pressure Fluctuation Characteristics in the Draft Tube

The temporal fluctuations in flow pressure significantly influence the structural loading characteristics of the runner and the vibration behaviors of the shafting system in a pump-turbine. Consequently, this section employs the Fast Fourier Transform (FFT) to process the raw pressure fluctuation data, aiming to analyze the time–frequency characteristics of the unit. The spatial distribution of the pressure monitoring points throughout the entire flow passage is illustrated in Figure 16. A total of 10 monitoring points are arranged upstream of the runner, all of which are situated on the XY plane at Z = 0 m. Specifically, monitoring points V1 to V3 are located within the volute region, GV1 to GV4 are distributed across the stay vane and guide vane regions, and VL1 to VL3 are positioned inside the vaneless space between the runner and the guide vanes. Within the draft tube region, monitoring points DT1 to DT4 are deployed, where DT1 and DT2 are located on a cross-sectional plane near the draft tube inlet, while DT3 and DT4 are situated on another plane within the elbow section.

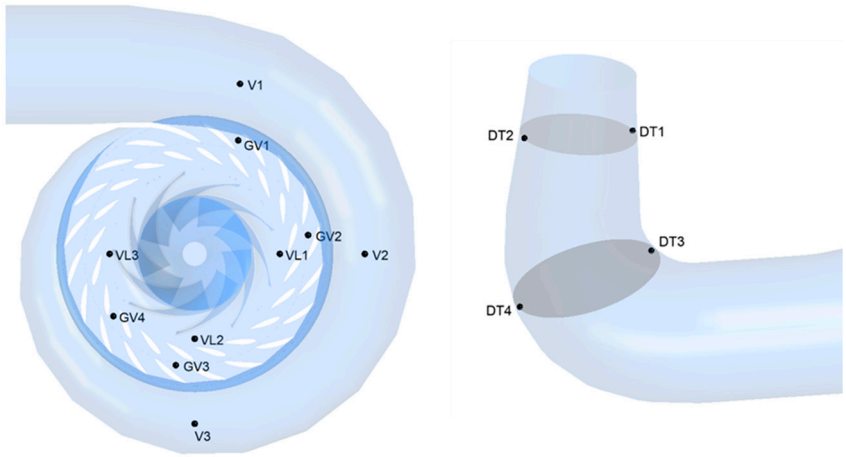


Figure 16. Pressure fluctuation monitoring point distribution.

To reduce errors inherent in pressure data itself, this section introduces the pressure difference P^* and the dimensionless number C_p to characterize the transient pressure fluctuation characteristics at each monitoring point.

$$p^* = p_i - p_{ave} \tag{12}$$

$$C_P = p^*/\rho g H \tag{13}$$

In the equation, P_i represents the measured pressure value at each time step, P_{ave} denotes the average of the measured pressure values, ρ is the density of water, g is the gravitational acceleration, and H is the head of 50 m.

The frequency-domain spectra for the respective monitoring points are obtained by performing the FFT on the dimensionless pressure fluctuation coefficient, C_p. In the present FFT analysis, the sampling interval is set equal to the time step of the numerical simulation, namely 2×10^{-4} s, which is equivalent to approximately 1.8° of runner rotation. The total sampling duration spans 2.5 s after the pump-turbine operation achieves a stable state, encompassing 60 complete runner revolution cycles. These sampling parameters are thoroughly sufficient to capture both the high-frequency pressure fluctuations induced by rotor-stator interaction (RSI) and the low-frequency pulsations triggered by the draft tube vortex rope.

To facilitate the comparative analysis of the pressure fluctuation plots, identical scale ranges are consistently applied to the subsequent figures. The fundamental runner rotation frequency, denoted as *fn* in the frequency-domain spectra, is 25 HZ.

The pressure fluctuations captured at the monitoring points inside the draft tube are presented in Figure 17 in both time and frequency domains for the 70% load case with different cavitation numbers. As observed from the spectra, under high cavitation number conditions, the dominant frequency at all monitoring points is $0.3f_n$. This specific frequency corresponds to the typical rotational frequency of a draft tube vortex rope. Conversely, when the unit operates under low cavitation number conditions, the time-domain waveforms exhibit more severe periodic distortions, accompanied by a significant increase in amplitude. In the frequency domain, the dominant frequency of the vortex rope shifts downward to $0.1f_n$, and a series of other complex low-frequency pulsation clusters emerge concurrently. This phenomenon demonstrates that the occurrence of cavitation induces a volumetric expansion of the vortex rope, which slows down its rotational speed and consequently reduces its characteristic frequency. Additionally, it is noteworthy that both the time-domain and frequency-domain fluctuations at monitoring point DT3, situated near the inner wall of the draft tube elbow section, are markedly more intense and complex than those at the other monitoring points. This discrepancy is likely attributable to the localized flow separation phenomenon occurring in this region.

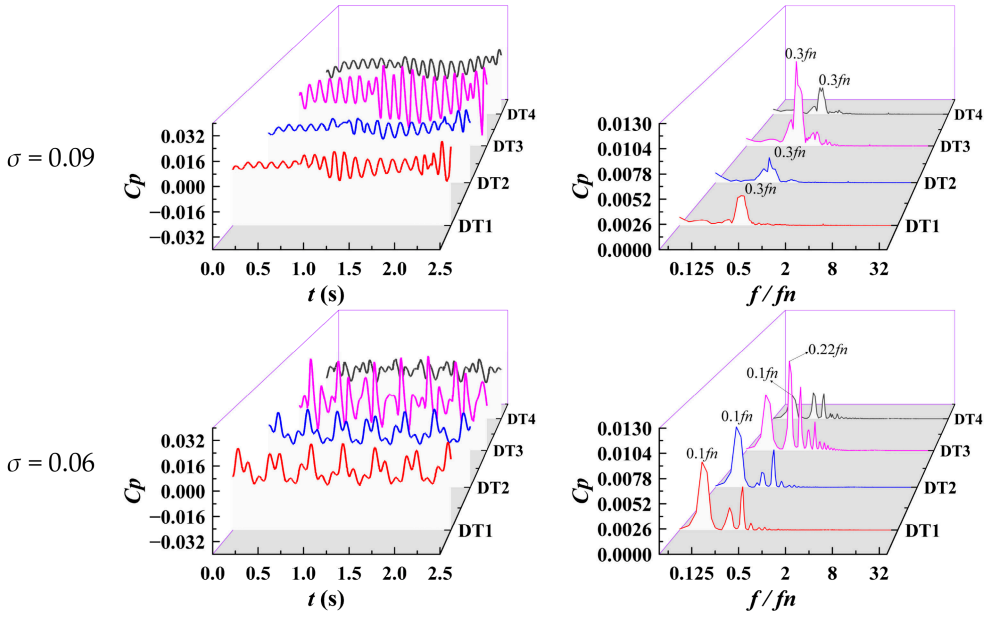


Figure 17. Draft tube pressure fluctuations in time and frequency domains at 70% load.

The pressure fluctuations captured at the monitoring points inside the draft tube are presented in Figure 18 in both time and frequency domains for the 90% load case with different cavitation numbers. As the operating load approaches the optimal efficiency point and the vortex rope weakens, the pressure fluctuations inside the draft tube gradually become quiescent. Under high cavitation number conditions, the time-domain waveforms at all monitoring points tend to be smooth and flat, while the corresponding frequency-domain spectra remain virtually featureless, with no distinct peaks. Conversely, for the low cavitation number conditions, minor low-frequency components re-emerge in the frequency-domain spectra.

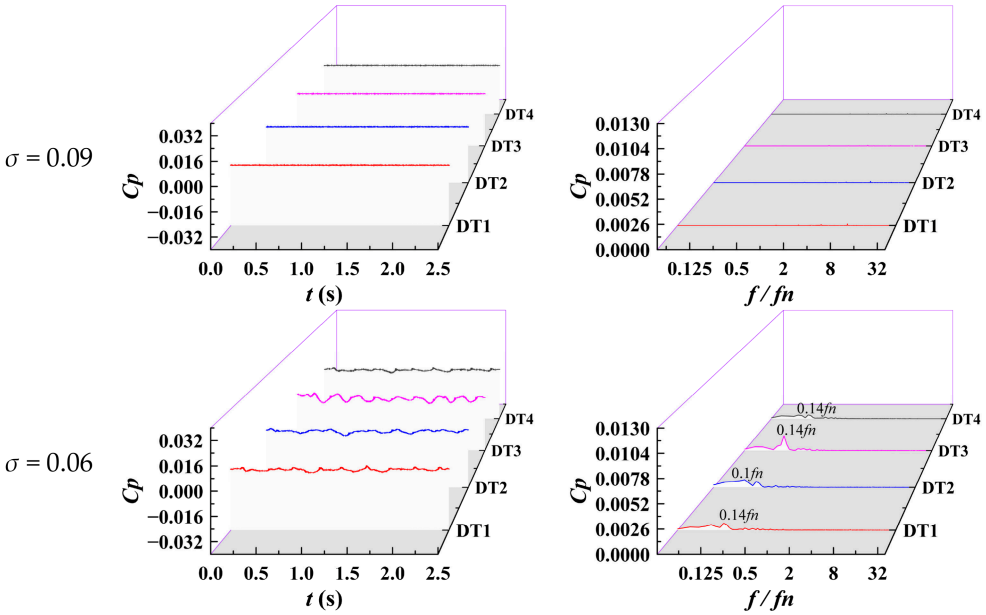


Figure 18. Draft tube pressure fluctuations in time and frequency domains at 90% load.

The pressure fluctuations captured at the monitoring points inside the draft tube are presented in Figure 19 in both time and frequency domains for the 100% load case with different cavitation numbers. The time–frequency characteristics under this operating condition exhibit a highly comparable trend to those of the preceding case (90% load), with only a minor incremental increase in the pulsation amplitude. Combined with the internal flow field analysis presented in the previous section, the expansion and contraction of the straight conical vortex rope likewise generate low-frequency pressure fluctuations. However, compared to the 70% partial load condition, the resulting pulsation amplitude remains remarkably small.

In summary, the analysis of the time–frequency characteristics elucidates the evolution patterns of pressure fluctuations within the draft tube. Under the 70% partial load condition, the dynamic motion of the eccentric vortex rope inside the draft tube generates highly intense low-frequency pressure pulsations. This low-frequency disturbance propagates upstream, directly influencing various regions of the flow passage. Conversely, under the 90% load condition near the optimal efficiency point, the internal flow field exhibits exceptional hydraulic stability. For the 100% rated load condition, although low-frequency pulsations are likewise generated within the draft tube, their overall amplitude levels are substantially mitigated.

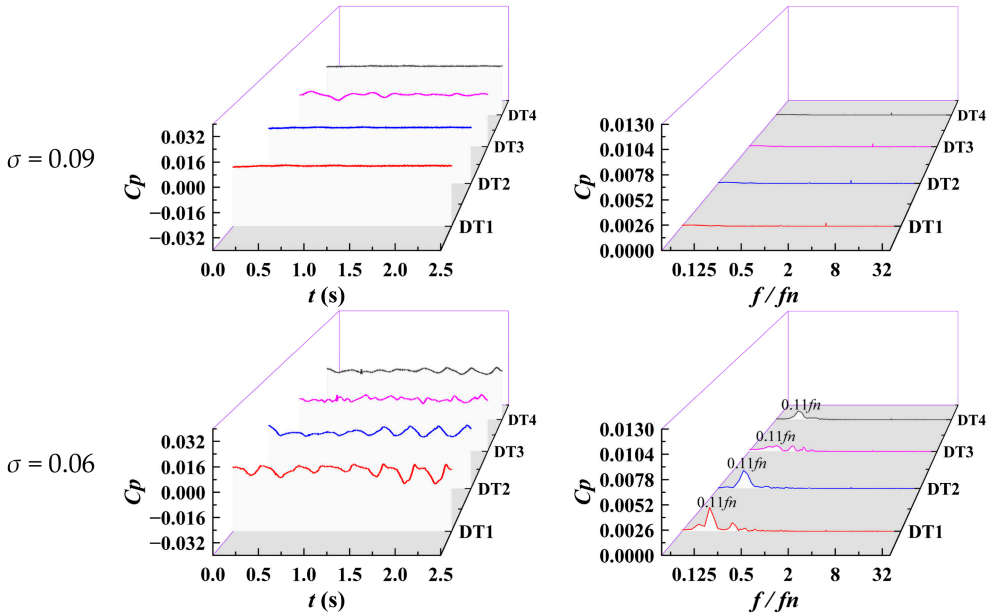


Figure 19. Draft tube pressure fluctuations in time and frequency domains at 100% load.

4.3. Structural Loading Characteristics of the Runner

The structural loading characteristics of the runner are intimately correlated with the energy conversion processes of the pump-turbine, directly determining the operational stability of the unit. Consequently, this section conducts an in-depth analysis of the runner loading characteristics. To minimize the inherent errors associated with the raw data, this section introduces the hydraulic exciting force difference, denoted as F^*, and the dimensionless force coefficient, Fr, to characterize the fluctuation features of the transient hydraulic exciting forces:

$$F^* = F_i - F_{ave} \tag{14}$$

$$Fr = F^*/F_{ave} \tag{15}$$

Figures 20 and 21 illustrate the frequency-domain spectra of the radial force under different load conditions. As observed from the spectra, the dominant frequency of the radial force under the 70% partial load condition is characterized by a low-frequency component, accompanied by the blade passing frequency ($9f_n$) and its higher harmonics. This dynamic loading characteristic of the runner strictly corroborates the previously discussed internal flow field findings. As the unit shifts to the 90% load condition, the magnitude of the low-frequency component within the radial force spectrum decreases substantially; consequently, the dominant frequency manifests as a high-frequency component with a relatively low amplitude. Furthermore, examining the frequency-domain spectrum under the 100% load condition reveals that the dominant frequency remains governed by the blade passing frequency and its higher harmonics. Finally, a cross-sectional comparison of the radial loading behaviors indicates that a reduction in the cavitation number consistently exacerbates the fluctuation severity of the runner forces, while simultaneously inducing the emergence of low-frequency components across all evaluated operating conditions.

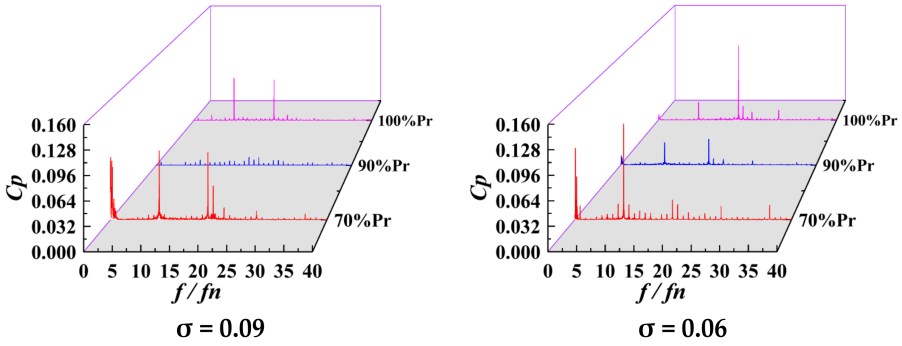


Figure 20. Frequency-domain spectra of runner X-direction forces under different loads.

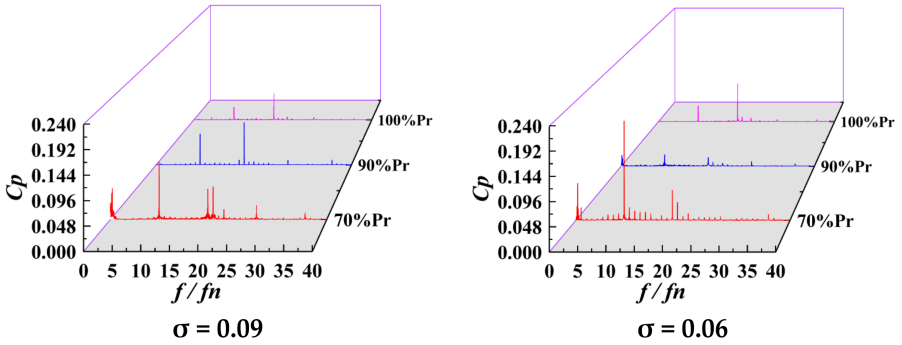


Figure 21. Frequency-domain spectra of runner Y-direction forces under different loads.

Subsequently, the stress characteristics of the runner blades are analyzed. Figure 22 illustrates the von Mises equivalent stress contours on the pressure side (PS) and suction side (SS) of the runner blades under the 70% load condition across varying cavitation numbers, with the left and right columns representing the PS and SS distributions, respectively. As observed from the contours, for both the PS and SS, the high-stress zones are consistently concentrated at the blade root regions, specifically at the junctions where the leading and trailing edges intersect with the crown and band. Comparing the loading conditions on both sides of the blade reveals that, under identical operating conditions, the stress exacerbation severity on the suction side is remarkably higher than that on the pressure side. Furthermore, the occurrence of cavitation significantly elevates the peak stress values under this specific operating condition.

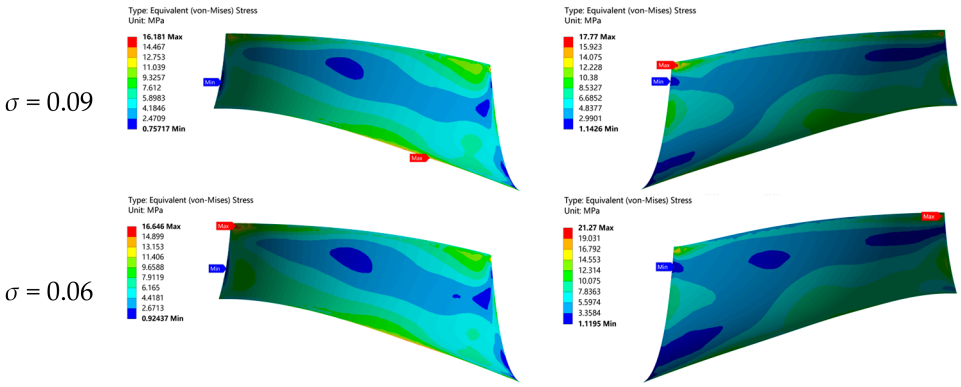


Figure 22. Blade surface stress distributions under the 70% load condition.

Figure 23 illustrates the von Mises equivalent stress contours on the pressure side and suction side of the runner blades under the 90% load condition across varying cavitation numbers. As observed from the contours, the spatial locations of the high-stress zones

remain unaltered. However, it is noteworthy that when the cavitation number decreases under this specific operating condition, a phenomenon contrary to the tendency observed in the preceding case occurs; specifically, the peak stress values of the runner blades experience a distinct reduction.

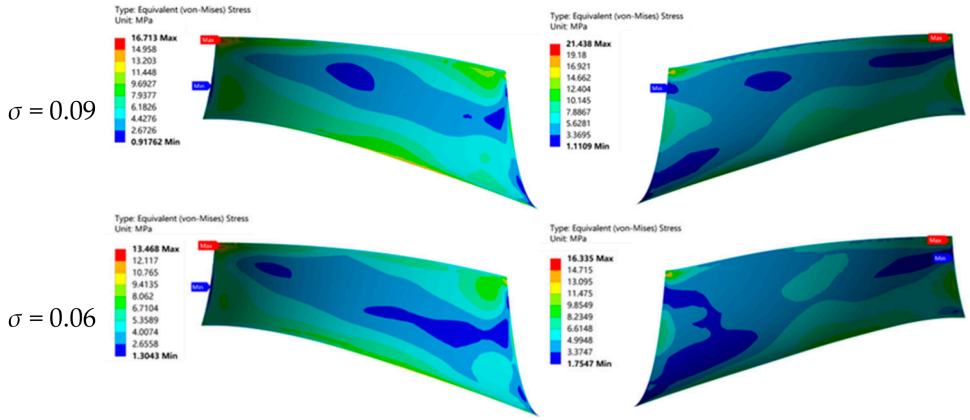


Figure 23. Blade surface stress distributions under the 90% load condition.

Figure 24 illustrates the von Mises equivalent stress contours on the pressure side and suction side of the runner blades under the 100% load condition across varying cavitation numbers. As observed from the contours, the stress concentration severity under this operating condition is mitigated to a certain extent. However, consistent with the observations at the 90% load, a lower cavitation number still corresponds to reduced peak stress levels on the blade surfaces. The reoccurrence of this phenomenon demonstrates that under higher load conditions, the onset and development of cavitation exert a beneficial mitigating effect on blade stresses. This may be because when the local pressure drops to the vaporization pressure, it becomes locked in place and cannot decrease any further. This limits the maximum pressure difference between the pressure side and the suction side of the blade, thereby directly reducing the peak stresses in the blade.

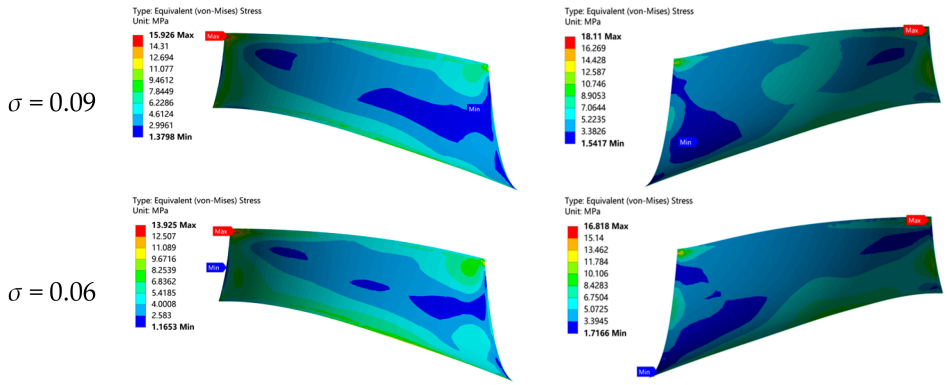


Figure 24. Blade surface stress distributions under the 100% load condition.

4.4. Vibration Characteristics of the Shafting System

Figure 25 illustrates the shaft orbit trajectories and displacement frequency-domain spectra at the turbine guide bearing under the 70% load condition across varying cavitation numbers. As observed from the spectra, the fundamental rotation frequency, f_n, consistently maintains a dominant position, demonstrating that mass eccentricity and hydraulic asymmetry of the shafting system constitute the primary components of shaft vibrations. Under high cavitation number conditions, the geometric shape of the shaft orbit trajectory exhibits an irregular, approximate elliptical profile. Conversely, as the cavitation number

decreases, the trajectory path becomes increasingly chaotic, accompanied by a discernible increase in displacement magnitude. Additionally, a distinct drift in the orbit trajectory is observable, with the entire trajectory positioning shifting toward the positive directions of both the X- and Y-axes. Furthermore, examining the frequency-domain spectra reveals that low-frequency peaks emerge in both the X- and Y-direction plots under both cavitation conditions, which precisely correspond to the previously identified low-frequency components within the draft tube. Although the amplitudes of these low-frequency components remain relatively low compared to the fundamental rotation frequency, the coexistence of such composite frequencies inevitably exacerbates the structural degradation of the shafting vibration state.

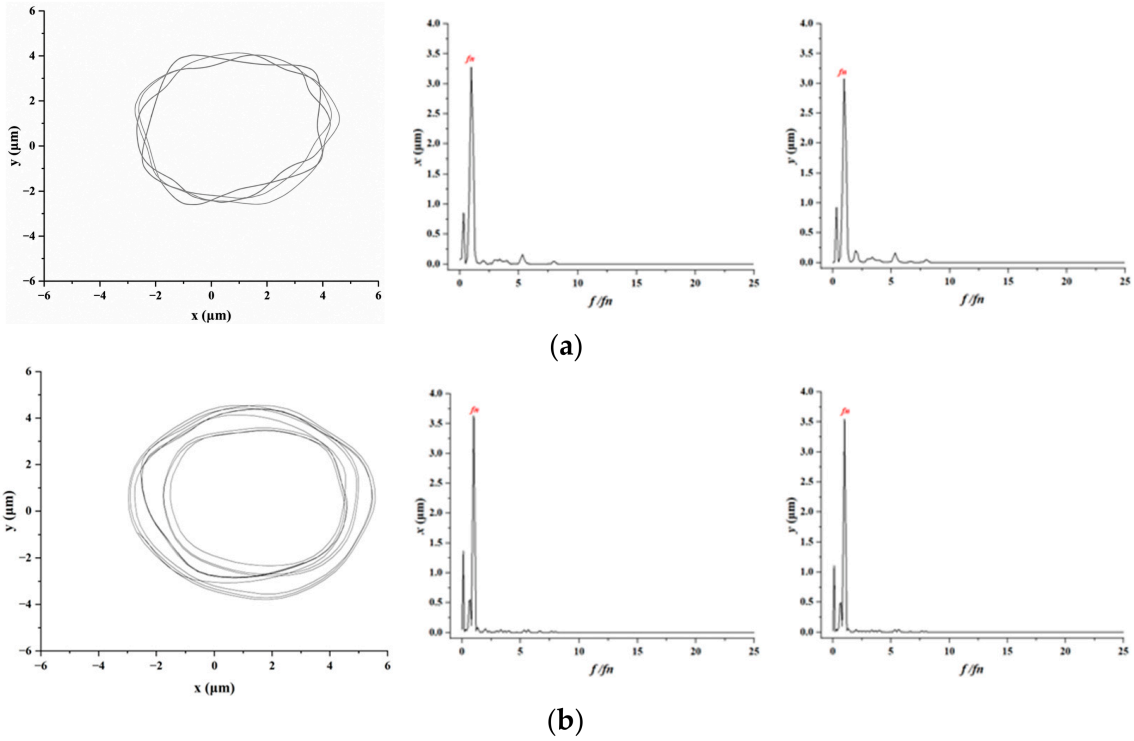


Figure 25. Shaft orbits and displacement spectra at 70% load: (**a**) σ = 0.09; (**b**) σ = 0.06.

Figure 26 illustrates the shaft orbit trajectories and displacement frequency-domain spectra at the turbine guide bearing under the 90% load condition across varying cavitation numbers. As observed from the displacement spectra, the fundamental rotation frequency, f_n, consistently maintains a dominant position under all evaluated cavitation conditions, with low-frequency pulsation components being virtually non-existent. Correspondingly, examining the shaft orbits reveals that the high cavitation number condition exhibits a highly standardized, regular elliptical geometry. Conversely, under the low cavitation number condition, the shaft orbit experiences a slight dilation and overlap phenomenon, though the overall trajectory remains fundamentally ordered. Concurrently, the displacement magnitude further diminishes under this load, yielding the lowest vibration levels among all evaluated operating conditions. Furthermore, the orbit trajectories exhibit minimal orbital drift, demonstrating the exceptional operational stability of the entire shafting system. This dynamic behavior highlights the highly stable internal flow field under the 90% load condition, where the draft tube vortex rope manifests as a slender, straight conical core that exerts a negligible impact on the radial vibrations of the unit.

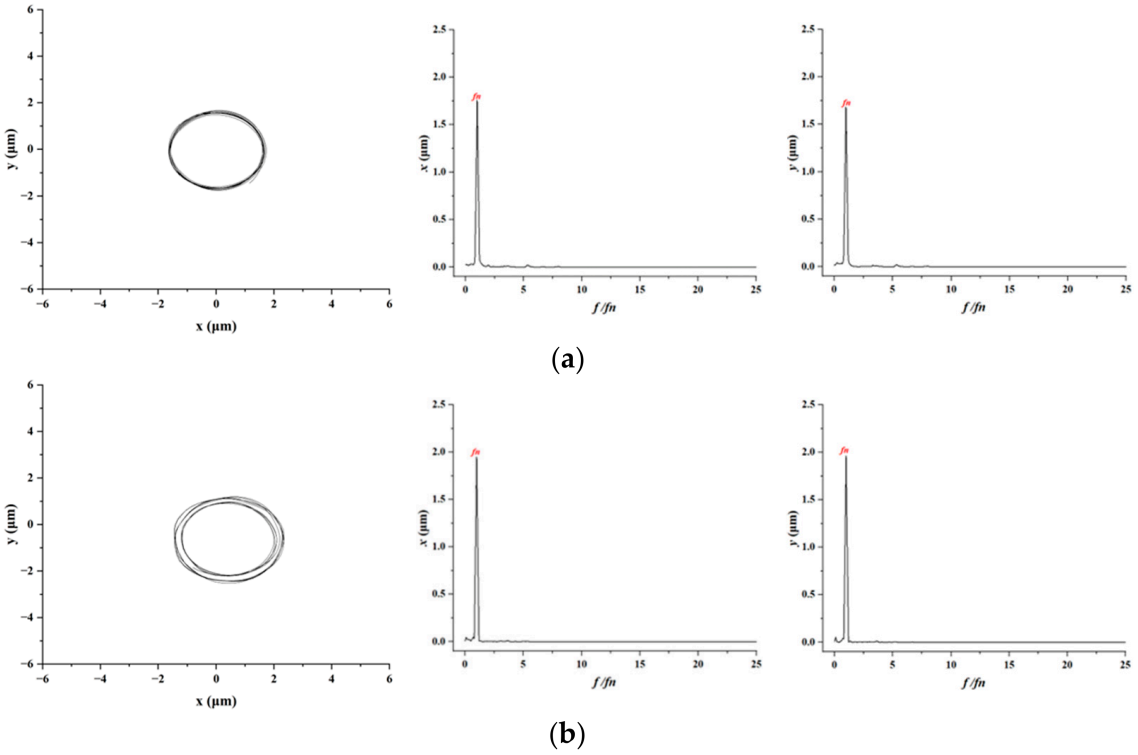


Figure 26. Shaft orbits and displacement spectra at 90% load: (**a**) σ = 0.09; (**b**) σ = 0.06.

Figure 27 illustrates the shaft orbit trajectories and displacement frequency-domain spectra at the turbine guide bearing under the 100% load condition across varying cavitation numbers. The dominant frequency in the displacement spectra remains governed by the fundamental rotation frequency, f_n, with no distinct low-frequency components observed. Although the preceding internal flow field analysis indicates the existence of low-frequency pulsations within the draft tube under this operating condition, their impact on the radial vibrations remains minimal due to their extremely low amplitudes and the straight conical morphology of the vortex rope. Consequently, the shaft orbit trajectories under this specific load condition still maintain a regular elliptical shape. However, the displacement magnitude exhibits a certain increase compared to the preceding case (90% load), which is primarily attributable to the corresponding elevation in the flow rate and output power. Conversely, the occurrence of cavitation exerts a negligible influence on the overall vibration characteristics under this operating condition.

The preceding investigation has elucidated the vibration characteristics of the shafting system under fixed structural stiffness parameters, identifying the 70% partial load condition as the most severe operating scenario regarding shaft vibrations. To further clarify the dynamic capability of each support bearing in resisting fluid-induced exciting forces, this section conducts a sensitivity analysis concerning the radial support stiffness of the shafting system. Utilizing the 70% load condition with a low cavitation number and the 100% load condition with a low cavitation number as the baseline cases, the control variable method is implemented to sequentially adjust the equivalent radial stiffness of the three primary bearings, namely the upper guide bearing, the lower guide bearing, and the turbine guide bearing. Specifically, Cases 1 and 2 represent a 50% decrease and a 50% increase in the stiffness of the upper guide bearing, respectively; Cases 3 and 4 correspond to a 50% decrease and a 50% increase in the stiffness of the lower guide bearing, respectively; and Cases 5 and 6 denote a 50% decrease and a 50% increase in the stiffness of the turbine guide bearing, respectively.

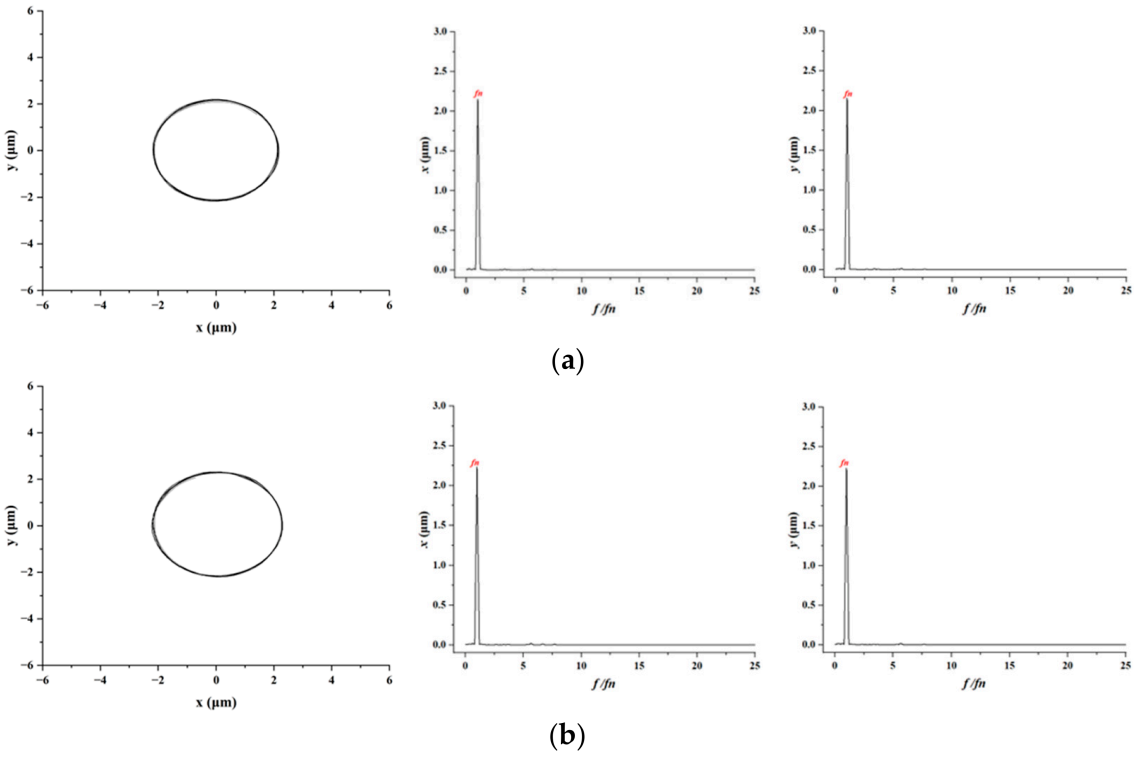


Figure 27. Shaft orbits and displacement spectra at 100% load: (**a**) σ = 0.09; (**b**) σ = 0.06.

Figure 28 statistically presents the relative change rates of the shaft runout values for the six groups of altered stiffness cases relative to the baseline cases under both the 70% and 100% load conditions. As observed from the diagram, under both the 70% and 100% load conditions, reducing the stiffness of the turbine guide bearing results in a substantial growth in the shaft runout along both the X- and Y-directions, with the maximum relative change rate reaching approximately 100%. Conversely, increasing the stiffness of the turbine guide bearing decreases the shaft runout by 30% to 40% under both operating conditions. Except for Case 3 under the 70% load condition, the relative change rates of the shaft runout induced by the stiffness variations of the upper and lower guide bearings are remarkably weak, remaining essentially within the engineering error margin.

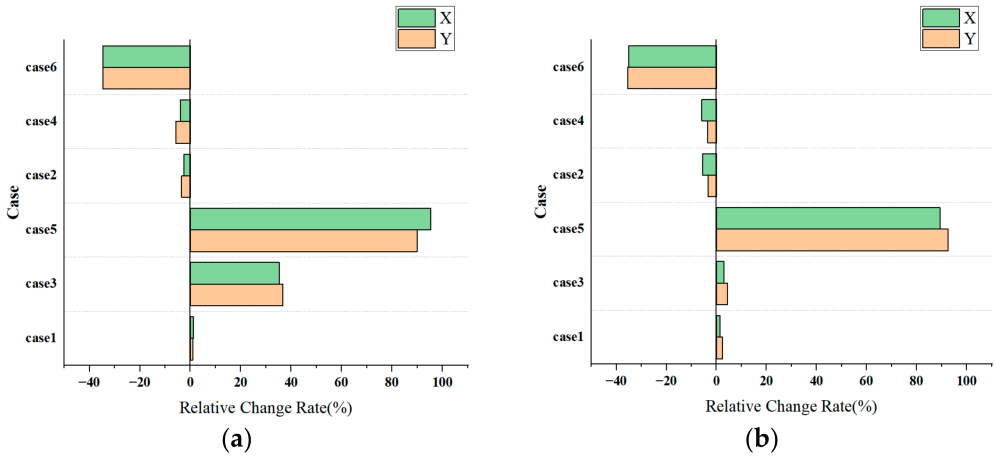


Figure 28. Comparison of shaft runout change rates under varying stiffness conditions: (**a**) 70% load; (**b**) 100% load.

5. Conclusions

This study systematically investigates the runner dynamics and shafting vibration characteristics of a pump-turbine across various operating loads and cavitation numbers based on a fluid–structure interaction approach. Following a comprehensive evaluation of the internal flow structures, pressure pulsations, and structural responses, the primary conclusions are summarized as follows:

(1) The morphology of the draft tube vortex rope is highly dependent on the operating load, which directly dictates the frequency-domain characteristics of the flow field pressure pulsations. Under the 70% partial load, the residual circulation creates an eccentric helical vortex rope that induces intense low-frequency pressure pulsations at a dominant frequency of $0.3f_n$, which further shifts downward to $0.1f_n$ due to cavitation expansion. In contrast, under the 90% and 100% load conditions, the vortex rope manifests as a symmetric, straight conical structure rotating around the centerline, restricting the resulting low-frequency pulsation amplitudes to a minimal level.

(2) The structural loading behaviors and dynamic stress distributions of the runner blades are intimately correlated with the localized flow patterns. Under the 70% load condition, the occurrence of cavitation elevates the peak stress values of the blades. Conversely, under the 90% and 100% load conditions, a reduction in the cavitation number consistently leads to a distinct reduction in the blade surface peak stress magnitude.

(3) The dominant frequency of the shafting radial vibrations is governed by the fundamental rotation frequency, f_n, though its macroscopic stability is heavily modulated by the downstream hydraulic excitations. Under the 70% load condition, the upstream propagation of the draft tube low-frequency pulsations leads to chaotic shaft orbits and pronounced directional drifts at the turbine guide bearing, whereas regular elliptical trajectories with minimal drift are maintained under the 90% and 100% loads. Furthermore, stiffness sensitivity analysis reveals that the relative change rates of the shaft runout are exceptionally sensitive to the equivalent radial stiffness of the turbine guide bearing.

Author Contributions: Conceptualization, Y.L.; methodology, L.C.; validation, A.Y. and L.D.; formal analysis, A.Y.; investigation, Y.L.; data curation, L.C.; writing—original draft preparation, Y.L. and L.C.; writing—review and editing, A.Y.; supervision, A.Y.; project administration, A.Y.; funding acquisition, A.Y. All authors have read and agreed to the published version of the manuscript.

Funding: The authors declare that this study received funding from Shanghai Investigation, Design & Research Institute Co., Ltd. (No. 2022SD(83)-010).

Data Availability Statement: The original contributions presented in this study are included in the article. Further inquiries can be directed to the corresponding author.

Conflicts of Interest: Author Yanhao Li was employed by Shanghai Investigation, Design & Research Institute Co., Ltd. The authors declare that this study received funding from Shanghai Investigation, Design & Research Institute Co., Ltd. The funder was not involved in the study design, collection, analysis, interpretation of data, the writing of this article or the decision to submit it for publication.

References

1. Lai, X.; Chen, X.; Liang, Q.; Ye, D.; Gou, Q.; Wang, R.; Yan, Y. Experimental and numerical investigation of vortex flows and pressure fluctuations in a high-head pump-turbine. *Renew. Energy* **2023**, *211*, 236–247. [CrossRef]
2. Shang, L.; Zhu, J.; Huang, X.; Gao, S.; Wang, Z.; Liu, J. Fluid-structure interactions in pump-turbines: A comprehensive review. *Processes* **2025**, *13*, 2321. [CrossRef]
3. Birajdar, R.; Keste, A. Prediction of flow-induced vibrations due to impeller hydraulic unbalance in vertical turbine pumps using one-way fluid-structure interaction. *J. Vib. Eng. Technol.* **2020**, *8*, 417–430.

4. Xue, Y.; Jiao, Y.; Cheng, C.; Wang, S.; Yang, B.; Li, H.; Li, W. Numerical and experimental study of structural vibrations in pump turbines. *Energy Rep.* **2025**, *14*, 1981–1992. [CrossRef]
5. Liu, J.T.; Liu, S.H.; Sun, Y.K.; Wu, Y.L.; Wang, L.Q. Numerical study of vortex rope during load rejection of a prototype pump-turbine. *IOP Conf. Ser. Earth Environ. Sci.* **2012**, *15*, 032044. [CrossRef]
6. Lai, X.D.; Liang, Q.W.; Ye, D.X.; Chen, X.M.; Xia, M.M. Experimental investigation of flows inside draft tube of a high-head pump-turbine. *Renew. Energy* **2019**, *133*, 731–742. [CrossRef]
7. Kim, S.J.; Suh, J.W.; Choi, Y.S.; Park, J.; Park, N.H.; Kim, J.H. Inter-blade vortex and vortex rope characteristics of a pump-turbine in turbine mode under low flow rate conditions. *Water* **2019**, *11*, 2554. [CrossRef]
8. He, Q.; Huang, X.; Bi, H.; Yang, M.; Yang, H.; Wang, Z. Draft tube vortex rope analysis of a pump-turbine unit under different operating conditions. *IOP Conf. Ser. Earth Environ. Sci.* **2022**, *1079*, 012012. [CrossRef]
9. Wang, H.; Zhou, D.; Guo, J.; Xu, L. Analysis of hydraulic losses in vortex rope inside the draft tube of francis pump-turbine based on entropy production theory. *Machines* **2023**, *11*, 965. [CrossRef]
10. Yu, A.; Tang, Y.; Liang, J.; Chen, P.; Zhang, Y.; Yang, C. Numerical investigation of the vorticity transportation and energy dissipation in a variable speed pump-turbine. *J. Energy Storage* **2024**, *93*, 112392. [CrossRef]
11. Liu, G.; Sun, L.; Guo, P.; Li, Y.; Wang, W.; Wang, Z. Coherent structure analysis of double-helix vortex rope in pump turbine operating in turbine mode based on POD and DMD. *J. Energy Storage* **2025**, *128*, 117144. [CrossRef]
12. Zhu, D.; Xiao, R.; Liu, W. Influence of leading-edge cavitation on impeller blade axial force in the pump mode of reversible pump-turbine. *Renew. Energy* **2021**, *163*, 939–949. [CrossRef]
13. Xin, L.; Li, Q.; Chen, X. Study on clearance flow distortion and associated force response in pump-turbines operating under S-characteristic conditions. *J. Energy Storage* **2026**, *153*, 121027. [CrossRef]
14. Hou, X.; Cheng, Y.; Yang, Z.; Liu, K.; Zhang, X.; Liu, D. Influence of clearance flow on dynamic hydraulic forces of pump-turbine during runaway transient process. *Energies* **2021**, *14*, 2830. [CrossRef]
15. Chen, F.; Bi, H.; Ahn, S.H.; Mao, Z.; Luo, Y.; Wang, Z. Investigation on dynamic stresses of pump-turbine runner during start up in turbine mode. *Processes* **2021**, *9*, 499. [CrossRef]
16. Li, X.; Cao, J.; Zhuang, J.; Wu, T.; Zheng, H.; Wang, Y.; Zheng, W.; Lin, G.; Wang, Z. Effect of Operating Head on Dynamic Behavior of a Pump–Turbine Runner in Turbine Mode. *Energies* **2022**, *15*, 4004. [CrossRef]
17. Guo, J.; Zhou, D.; Chen, H.; Wang, H. Flow-induced vibration analysis in a pump-turbine runner under transient operating conditions. *Eng. Appl. Comput. Fluid Mech.* **2023**, *17*, 2266662. [CrossRef]
18. Lund, J.W. Spring and damping coefficients for the tilting-pad journal bearing. *Asle Trans.* **1964**, *7*, 342–352. [CrossRef]
19. Lund, J.W. The stability of an elastic rotor in journal bearings with flexible, damped supports. *J. Appl. Mech.* **1965**, *32*, 911–920. [CrossRef]
20. Bently, D.E.; Goldman, P.; YuJ, J. The advantages of dynamic stiffness parametersover classical bearing coefficients. *Orbit* **2001**, *3*, 23–29.
21. Pandya, H.R.; Pandya, J.G.; Acharya, G.D. Vibration Analysis of Pump Shaft Using Finite Element Analysis Software: A Review. *Trends Mech. Eng. Technol.* **2018**, *8*, 46–54.
22. Liu, X.; Pang, J.; Li, L.; Zhao, W.; Wang, Y.; Yan, D.; Zhou, L.; Wang, Z. Comparative study on numerical calculation of modal characteristics of pump-turbine shaft system. *J. Mar. Sci. Eng.* **2023**, *11*, 2068. [CrossRef]
23. Cao, J.; Luo, Y.; Liu, X.; Presas, A.; Deng, L.; Zhao, W.; Xia, M.; Wang, Z. Numerical theory and method on the modal behavior of a pump-turbine rotor system considering gyro-effect and added mass effect. *J. Energy Storage* **2024**, *85*, 111064. [CrossRef]
24. Wang, L.; Yu, S.; Wang, Z. Modal characteristics analysis of a variable-speed pump-turbine rotor system: A perspective of resonance. *J. Phys. Conf. Ser.* **2024**, *2854*, 012084. [CrossRef]
25. Kong, L.; Cao, J.; Li, X.; Zhou, X.; Hu, H.; Wang, T.; Gui, S.; Lai, W.; Zhu, Z.; Wang, Z.; et al. Numerical analysis on the hydraulic thrust and dynamic response characteristics of a turbine pump. *Energies* **2022**, *15*, 1580. [CrossRef]
26. Mao, Z.; Tao, R.; Chen, F.; Bi, H.; Cao, J.; Luo, Y.; Fan, H.; Wang, Z. Investigation of the starting-up axial hydraulic force and structure characteristics of pump turbine in pump mode. *J. Mar. Sci. Eng.* **2021**, *9*, 158. [CrossRef]
27. Feng, C.; Sun, J.; Zhang, Y.; Zheng, Y. A novel multi-excitation transient vibration framework for coupling three-and one-dimensional pumped storage hydropower shafting systems. *Phys. Fluids* **2024**, *36*, 105143. [CrossRef]
28. Zhou, W.J.; Wei, X.S.; Wu, G.K.; Liu, W.J.; Wang, L.Q. Numerical research on dynamic lateral vibration of a pumpturbine'sshaft system. *J. Eng. Res.* **2015**, *3*, 38. [CrossRef]
29. Zhang, J.; Ma, Z.; Wang, X.; Wu, Q.; Zhang, L. Transient vibration of shafting in coupled hydraulic-mechanical-electrical-structural system for hydropower station during start-up process. *Appl. Math. Model.* **2023**, *124*, 860–880. [CrossRef]
30. Shi, Y.; Shen, J.; Guo, W.; Li, C.; Zheng, Y.; Zhao, Z.; Zhou, J.; Zhang, Y. The nonlinear dynamic characteristics analysis and vibration reduction control of the shafting system of a hydropower unit. *Int. J. Non-Linear Mech.* **2022**, *146*, 104166. [CrossRef]
31. Ansari, B.; Aligholami, M.; Rostamzadeh Khosroshahi, A. An experimental and numerical investigation into using hydropower plant on oil transmission lines. *Energy Sci. Eng.* **2022**, *10*, 4397–4410. [CrossRef]

32. Sun, L.; Guo, P.; Luo, X. Numerical investigation on inter-blade cavitation vortex in a Franics turbine. *Renew. Energy* **2020**, *158*, 64–74. [CrossRef]
33. Luo, X.; Yu, A.; Ji, B.; Wu, Y.; Tsujimoto, Y. Unsteady vortical flow simulation in a Francis turbine with special emphasis on vortex rope behavior and pressure fluctuation alleviation. *Proc. Inst. Mech. Eng. Part A J. Power Energy* **2017**, *231*, 215–226. [CrossRef]

Disclaimer/Publisher's Note: The statements, opinions and data contained in all publications are solely those of the individual author(s) and contributor(s) and not of MDPI and/or the editor(s). MDPI and/or the editor(s) disclaim responsibility for any injury to people or property resulting from any ideas, methods, instructions or products referred to in the content.